Search for production of a Higgs boson and a single top quark in $\mu\mu$ final states in proton collisions from LHC

Hiram Ernesto Damián

Departmento de investigación en física
Universidad de Sonora

Para obtener el grado de:
Maestría en Ciencias (Física)

Hermosillo, Sonora

October 2019

I would like to dedicate this thesis to my loving mother . . .

Acknowledgements

And I would like to acknowledge ...

Abstract

I present a study on the production of tH in same sign dimuon channel $\mu \pm \mu \pm$ A likelihood scan is performed to show the probability of observation of the signal. By studying this process , I explore a Higgs production mechanism ,which it has not been observed yet experimentally. Simulation is used to predict sensitivity for the LHC high luminosity phase. This could help to obtain better limits for the production of tH. I also include the model $k_t = -1$, where k_t is the top higgs coupling parameter, for compare it with the standard model.

Table of contents

List of figures

List of tables

Chapter 1

Introduction

1.1   General objetive and motivations

Particle physics is a field of study of physics that studies the particles that create matter and its interactions to very small scale, even smaller than atoms. The particles analized in particle physics are the fundamental particles that compose the matter and the responsibles for all forces of nature. All thoses particles and their properties are grouped in a theory called the Standard Model. Standard Model (SM) is a theory that describes the fundamental forces (except gravity) and classify the elementary particles in bosons (entire spin) and fermions (half spin). The SM , created almost 50 years ago, has been the most successul theory in explain the phenomena in the subatomic world.

One of the particles of the SM, the Higgs Boson , was recently discovered in 2012 in the ATLAS and CMS experiments at CERN. The discovery of Higgs boson in proton proton collisions marked a new era in the particle physics due to its characteristic of giving the matter the property of mass, according to previous theories and predictions . Since then, people around the world are working in the Large Hadron Collider at CERN in order to detect the Higgs bosons in higher energies and differents Higgs production processes. Also the impact of Higgs is also important in cosmology, where theoretical investigations relate the Higgs boson and the cosmic inflation.

In the recent years, there have been many studies in the Higgs production processes at CERN in pp collisions , such as gluon fusion (ggF), VBF, WH, ZH and $t\bar{t}$H and people have obtained consistent results in the search of Higgs in those processes. In this work, we will analize the production of Higgs boson in association with a single top quark (tH) in proton-proton collisions with the CMS experiment of the LHC. The motivation of the work

25   is this mechanism of production of the Higgs boson has not been observed before by any
26   experiment. The exploration of Higgs production on the tH channel is subject relatively
27   new.
28   Many channels are yet out of reach experimentally. At the same time, many theoretical
29   proposals are yet to be put on test. It is possible that studies on the Higgs boson give
30   evidence of small deviations from the SM and test new physics that are beyond SM such
31   as String Theory and Supersymmetry.
32

1.2   The Standard Model

34   The SM, created in the decade of seventies, is a successful theory that explains the structure
35   of matter and the interactions of three of the four fundamental forces which are electro-
36   magnetic, strong and weak forces. The gravitational force is yet to be included due to the
37   scale of interaction with respect to the other 3. All the matter is composed of three kinds
38   of particles: leptons, quarks and bosons, also called mediators.
39

40   For the leptons we have electrons (e), muons (μ), and taus (τ) with charge -1 and their
41   neutrinos v_e, v_μ, v_τ, are chargeless particles. Leptons have their respective antiparticle;
42   same structure with opposite charge. All of them have a spin (intrinsic angular momentum)
43   of $\frac{1}{2}$. [7].
44

45   Quarks combine to form composite particles called hadrons. Quarks cannot be found
46   in isolation, they always exist in form of hadrons that can be mesons or baryons.
47   Mesons , are bosons made up of a quark-antiquark pair, such as pion (π) and kaon
48   (K).Mesons were theorized by Yukawa in 1937 and discovered in 1947 by Powell. [7]
49   Baryons are fermions made of 3 quarks. Examples of baryons are protons and neutrons.
50   Both particles can interact via strong force.
51

52   Quarks were first theorized by Murray Gell-Mann and George Zweig in 1964, were
53   introduced as parts of an ordering scheme for hadrons, and there was little evidence for
54   their physical existence until scattering experiments at the Stanford Linear Accelerator
55   Center in 1968.[7] There are 6 of them: up (1968), down (1968), strange (1968), charm
56   (theorized in 1970, discovered 1974), bottom (theorized 1973, discovered 1977), top
57   (theorized 1973, discovered 1995).
58

59   Quarks have characteristics such as electric charge, mass, color charge, and spin. The
60   quarks up, charm and top have in common a charge of $\frac{2}{3}$, while the down , strange and

61 bottom quarks have charge of $-\frac{1}{3}$. Among them , the top quark is the most massive of all,
62 while the up and down are the least massive. The lepton and quarks have their respective
63 antiparticle, which have the same mass, but inverted charge.

64 Some of the particles in the SM are not stable, so they decays and form particles with
65 lower masses. Other particles do not decay or their lifetimes are very long. The final states
66 can be represented with a Feynman diagram according to the SM vertices. [8]

Standard Model of Elementary Particles
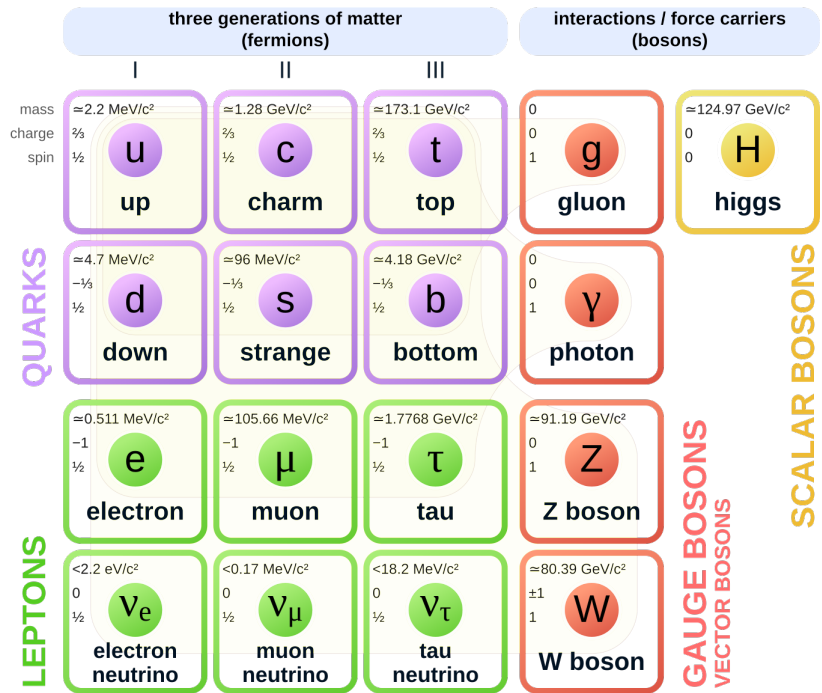
Fig. 1.1 Standard Model to date[1]

67

68   The last group of the family are the bosons,which have a spin 1 and 0. There are 5
69 bosons: $W^{\pm}$, Z with neutral charge are responsibles for weak force; photon, a massless
70 particle, is responsible for electromagnetic force; gluon which also massless, is related
71 to strong force and Higgs boson, recently discovered , is in charge of give the property
72 of mass to particles via Higgs mechanism. Bosons let other particles to interact, even
73 themselves, which is shown in the figure 1.2.

74 The W,Z and Higgs bosons, can interact with the most of the particles, while the gluon can
75 only interact with quarks and itself. Those bosons act as mediators in decays and creation
76 of complex particles, as mesons and baryons.

77

---

[1]Taken from Wikimedia. https://upload.wikimedia.org/wikipedia/commons/0/00/Standard_Model_of_Elementary_Particles.svg
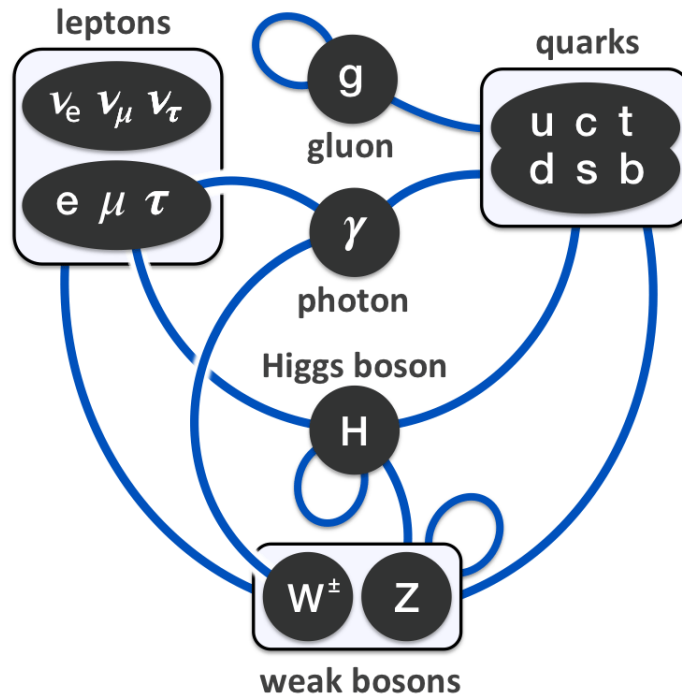
Fig. 1.2 Particle interactions in Standard model

There are experiments that detects particles around the world, such as the large hadron collider (LHC) in Europe, the Fermilab in United States of America, KEK in Japan, etc. More information about the LHC will be described in the next chapters.

Since quarks and gluons only exist in bound states, it is imposible to observe isolated quarks except the top quark, which decays before it has time to form a bound state. As two quarks are separated, the strong force between them increases which is equivalent to the potential energy increasing. This energy transforms into quark-anti-quark pairs.

The table 1.1 contains the characteristics of each particle in the SM. Note the distance column refers to particles moving with speeds near light speed. This column visualize the distance traveled in the predicted lifetime of the particle. And also give us a perspective of how hard is the detection of the particles due to lifetime. Stable lifetime means that the particles do not decay or can exist until they can interact with detectors.

Table 1.1 Table of particles in SM[6]. Stable means no decay, or lifetime almost infinite. Particles speeds at 0.998c

Particle	Mass (MeV/c^2)	Charge	spin	Lifetime (s)	Distance in lifetime (meters)
Up (u)	2.2	$\frac{2}{3}$	$\frac{1}{2}$	stable	-
Charm (c)	1280	$\frac{2}{3}$	$\frac{1}{2}$	1.1×10^{-12}	5.21×10^{-3}
Top (t)	173100	$\frac{2}{3}$	$\frac{1}{2}$	5×10^{-25}	2.37×10^{-15}
Down (d)	4.6	$-\frac{1}{3}$	$\frac{1}{2}$	Stable	-
Strange (s)	96	$-\frac{1}{3}$	$\frac{1}{2}$	1.24×10^{-8}	58.7
Bottom (b)	4180	$-\frac{1}{3}$	$\frac{1}{2}$	1.3×10^{-12}	6.16×10^{-3}
W	80379	± 1	1	3×10^{-25}	1.42×10^{-15}
Z	91187.6	0	1	3×10^{-25}	1.42×10^{-15}
Photon (γ)	0	0	1	Stable	-
Gluon (g)	0	0	1	Stable	-
Higgs (H)	125.18	0	0	1.56×10^{-22}	7.39×10^{-13}
Electron (e)	0.511	-1	$\frac{1}{2}$	Stable	-
Muon (μ)	105.7	-1	$\frac{1}{2}$	2.2×10^{-6}	10419.85
τ	1776.86	-1	$\frac{1}{2}$	2.9×10^{-13}	1.37×10^{-3}
ν_e ν_μ ν_τ	0	0	$\frac{1}{2}$	Stable	-

1.3   Higgs Boson

The Higgs is a boson with spin 0 and chargeless. First theorized in 1964 by a group of theoretical physicist composed by Peter Higgs, François Englert, Robert Brout, Gerald Guralnik, C. Richard Hagen, and Tom Kibble in separated groups. They formulated the Higgs mechanism that explain the generation of mass for the particles .

The theory also explains Higgs bosons give the mass to the particles via Higgs Field and the mass of Higgs boson itself. The Higgs boson was discovered recently on year 2012 in the experiments ATLAS and CMS at CERN. The experiment was a proton proton collision with center of mass energy of 7 and 8 TeV ,where investigators worked on the data and detecting various decay modes that generates final states such as WW, $\gamma\gamma$, ZZ, b$\bar{b}$ and $\tau\tau$ [9].

The mass of this boson has been measured and its production and decay rates are consistent with the SM prediction. The mass of the Higgs boson measured is approximately 125 MeV. The Higgs boson lifetime is 1.56×10^{-22}. That is why the Higgs boson was very difficult to detect in the particle detectors.

1.4 Top quark

The top quark is the most massive particle with a charge of 2/3 with spin of 1/2. First proposed by M. Kobayashi and T. Maskawa in 1973 to explain observed CP violations in Kaon decay[7]. On 1995, in the Tevatron at Fermilab in Illinois, the top quark was discovered via proton antiproton collisions with center of mass energy between 1.8 to 1.96 TeV in the CDF and D0 experiments.The top quark production process was via ggF, which generated a pair of $t\bar{t}$[10] . Since then,the properties of the top quark have been studied at the Tevatron Collider at Fermilab, and by the ATLAS and CMS experiments at the Large Hadron Collider (LHC) at CERN.

However, the top quark often receives special attention in new physics models because its mass requires near unity coupling to the Higgs boson [10]. As shown in table 1.1, the top quark lifetime is so small that they decay before they can hadronise, that is to say, the process to create hadrons from quarks and gluons.

One of interesting the properties of top quark is its mass. The top quark mass is a free parameter in the SM and was extracted using indirect measurements and relying on SM calculations. The measured value of top quark mass is of 173 Gev[6]. The top quark mass is a very important parameter that puts a constraint in the Higgs boson mass and also takes an important role in electroweak symmetry breaking[10].

The production of top quark can be generated in differents ways. In tevatron and LHC, the production of $t\bar{t}$ comes from ggF (gluon gluon fusion) via strong force. Even it is posible to create a single top quark in the LHC via electroweak interactions (with a W boson) [11]. The top quark, due to its big mass, always decays into a W boson and a b quark. But since the W boson have various decays, the top quark can generate many posible particles, acording to W boson decays. Some posible decays of top quark is the decay to a lepton such as muon, electron or tau and their neutrinos .

₁₃₇ **1.5   Higgs mechanism**

₁₃₈ In the SM, mathematically the particles are described in form of fields. The SM for
₁₃₉ electroweak interactions is described as a gauge theory with a symmetry group SU(2)⊗U(1)
₁₄₀ that describes the weak and electromagnetic interactions due to the exchange of spin 1
₁₄₁ gauge fields($W^{\pm}$,Z) for the weak part and a photon for the electromagnetic part. The Higgs
₁₄₂ mechanism give bosons and fermions their mass.

The lagrangian for the electroweak part of SM

$$\mathscr{L}_{\text{EW}} = \mathscr{L}_{\text{gauge}} + \mathscr{L}_f + \mathscr{L}_{\text{Higgs}} + \mathscr{L}_{\text{Yukawa}} \tag{1.1}$$

The first term of the lagrangian refers to gauge bosons

$$\mathscr{L}_{\text{gauge}} = -\frac{1}{4}\left[F^{\mu\nu}F_{\mu\nu}\right] - \frac{1}{4}\left[\sum_i G^{i\mu\nu}G^i_{\mu\nu}\right] \tag{1.2}$$

where the F and G are

$$F^{\mu\nu} = \partial_\mu B_\nu - \partial_\nu B_\mu \tag{1.3}$$

$$G^{i\mu\nu} = \partial_\mu W^i_\nu - \partial_\nu W^i_\mu - g\varepsilon^{ijk}W^j_\mu W^k_\nu \tag{1.4}$$

₁₄₃ W^i (i=1,2,3) are three SU(2) gauge bosons and B is a U(1) gauge boson.[2] In the end,
₁₄₄ those gauge bosons, after introduce the Higgs mechanism, become the $W^{\pm}$, Z and γ vector
₁₄₅ boson [12, 13].

₁₄₆

The second term refers to kinematic energy of fermions

$$\mathscr{L}_f = \sum_{m=1}^3 \left(\bar{q}^m_L i\displaystyle{\not}D_L q^m_L + \bar{l}^m_L i\displaystyle{\not}D_L l^m_L + \bar{u}^m_R i\displaystyle{\not}D_R u^m_R + \bar{d}^m_R i\displaystyle{\not}D_R d^m_R + \bar{e}^m_R i\displaystyle{\not}D_R e^m_R\right) \tag{1.5}$$

---

[2]ε^{ijk} represents the Levi-Civita tensor, where $\varepsilon^{ijk} = \begin{cases} +1 & \text{for even permutation} \\ -1 & \text{for odd permutation} \\ 0 & \text{i=j, or j=k, or k=i} \end{cases}$.

where m is the family index, and L(R) refer to the left (right) handed particles.[3]. The gauge covariant derivatives are given by

$$D_L = \left(\partial_\mu + ig\sigma^i W_\mu^i + ig'YB_\mu \right) \tag{1.6}$$

$$D_R = \left(\partial_\mu + ig'YB_\mu \right) \tag{1.7}$$

where σ^i are the pauli matrices. L and R refers to left and right handed fields. The left handed fields for the first family are defined by the following doublets

$$q_L = \begin{pmatrix} u_L \\ d_L \end{pmatrix} \qquad l_L = \begin{pmatrix} \nu_{eL} \\ e_L^- \end{pmatrix} \tag{1.8}$$

and the right handed fields

$$u_R, d_R, e_R^- \tag{1.9}$$

The hypercharges Y depend of the particle type. For left handed

$$Y(l_L) = -\frac{1}{2} \quad Y(q_L) = \frac{1}{6} \tag{1.10}$$

for right handed

$$Y(e_R) = -1 \quad Y(u_R) = \frac{2}{3} \quad Y(d_R) = -\frac{1}{3} \tag{1.11}$$

The lagrangian for Higgs field

$$\mathscr{L}_{\text{Higgs}} = (D_\mu \Phi)^\dagger (D^\mu \Phi) - V(\Phi^\dagger \Phi) \tag{1.12}$$

where D_μ is a operator

$$D_\mu = \left(\partial_\mu + i\frac{1}{2}\sigma^i g W_\mu^i + i\frac{1}{2}g'B_\mu \right) \tag{1.13}$$

and the Higgs potential $V(\Phi^\dagger \Phi)$

$$V(\Phi^\dagger \Phi) = \mu^2 \Phi^\dagger \Phi + \frac{1}{2}\lambda(\Phi^\dagger \Phi)^2 \tag{1.14}$$

---

[3] $\bar{\psi}$ denotes the adjoint spinor $\bar{\psi} = \psi^\dagger \gamma^0$. $\slashed{D} = \gamma^\mu D_\mu$. γ are the Dirac matrices

147     $\Phi = \begin{pmatrix} \phi^+ \\ \phi^0 \end{pmatrix}$ is a SU(2) doublet of scalar fields. V is symmetrical under rotations in

148   Φ space and parameters λ and μ^2 are parameters of the potential. The Higgs potential for

149   $\mu^2 < 0$ and $\lambda > 0$ can be visualized in the figure 1.3
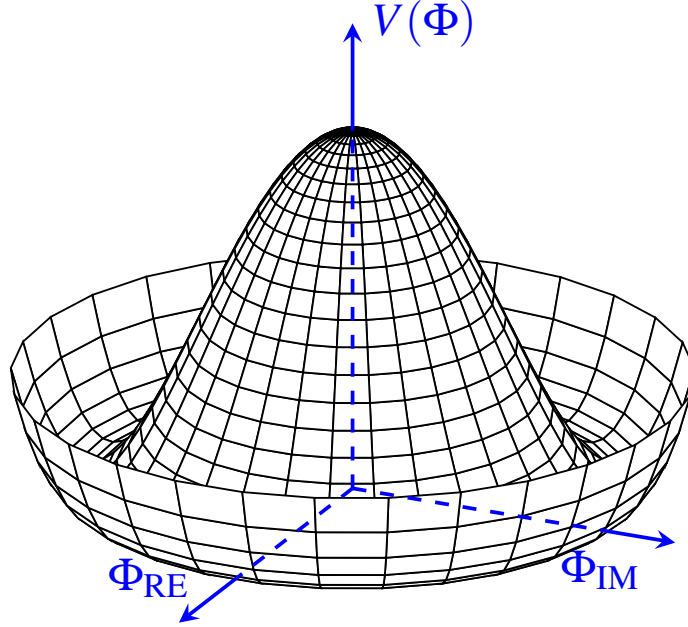
Fig. 1.3 Higgs potential $V(\Phi^\dagger \Phi)$ for $\mu^2 < 0$ and $\lambda > 0$ also called the mexican hat potential.

Electroweak symmetry breaking refers to the choice of ground state

$$\Phi_0 = \frac{1}{\sqrt{2}} \begin{pmatrix} 0 \\ v \end{pmatrix} \tag{1.15}$$

150   where $v = -\frac{\mu^2}{\sqrt{2}}$ is called the vacuum expectation value.

151

Taking 1.15 and substituting in $\mathscr{L}_{\text{Higgs}}$, we get

$$(D_\mu \Phi)^\dagger (D^\mu \Phi) = \frac{v^2}{8} \left(g^2((W_\mu^1)^2 + (W_\mu^2)^2) + (gW_\mu^3 - g'B_\mu)^2 \right) \tag{1.16}$$

we define the physical vector boson W_μ^-. W_μ^+ and Z

$$W_\mu^\pm = \frac{1}{\sqrt{2}}(W_\mu^1 \mp iW_\mu^2) \tag{1.17}$$

$$Z_\mu = \frac{1}{\sqrt{g^2 + g'^2}} \left(gW_\mu^3 - g'B_\mu \right) \tag{1.18}$$

Now introducing 1.17 and 1.18 in 1.16,

$$(D_\mu \Phi)^\dagger (D^\mu \Phi) = \frac{v^2}{8} \left(2g^2 W_\mu^+ W^{\mu -} + (g^2 + g'^2) Z_\mu Z^\mu \right) \qquad (1.19)$$

from the coeficients, we get the W and Z mass

$$m_W = \frac{gv}{2} \qquad m_Z = \frac{v}{2} \sqrt{g^2 + g'^2} \qquad (1.20)$$

The last part of the lagrangian is the Yukawa lagrangian

$$\mathscr{L}_{\text{yukawa}} = \sum_{m,n}^{3} \Gamma_{mn}^u \bar{q}_{m,L} \tilde{\Phi} u_{n,R} + \Gamma_{mn}^d \bar{q}_{m,L} \Phi d_{n,R} + \Gamma_{mn}^e \bar{l}_{m,L} \Phi e_{n,R} + h.c \qquad (1.21)$$

The matrices Γ_{mn} describe the so called Yukawa couplings between Higgs doublet Φ and the fermions.[4] The indices m and n mean sum over the families.

By using 1.15 it on $\mathscr{L}_{\text{yukawa}}$, it is obtained for u quark

$$\frac{\Gamma_{uu}^u v}{\sqrt{2}} (\bar{u}_L u_R + \bar{u}_R u_L)$$

from which the masses for the fermions shown to be proportional to the Yukawa couplings

$$m_u = -\frac{\Gamma_{uu}^u v}{\sqrt{2}}$$

---

[4]Here $\tilde{\Phi} = i\sigma^2 \Phi^\dagger = \begin{pmatrix} \phi^{0\dagger} \\ -\phi^- \end{pmatrix}$ is necessary for the correct transformation in the case of up quarks.
h.c refers to hermitian conjugate terms.

1.6   Higgs production mechanisms

During a particle collision, there are various ways that the Higgs boson can be created. The most common is the gluon gluon fusion process (ggF) which is the process which involve two gluons mediated by the exchange of a virtual, heavy top quarks. Another process is vector boson fusion (VBF), where two fermions interact via a vector boson (W or Z) and create a Higgs along with other particles. There is also the vector higgs process (VH), where the creation of particles using vector boson comes from a interaction between fermions and anti fermions[6]. These processes are shown in the figure 1.4

In the recent years, people have studied the top anti top Higgs ($t\bar{t}H$) process, in order to detect a Higgs boson, via multilepton signals [11]. In this process, the creation of a Higgs boson comes from a intection via $t\bar{t}$. In the figure 1.4, the $t\bar{t}H$ starts with 2 gluons which decay to two $t\bar{t}$ pairs and after that , the interaction $t\bar{t}$ generates a Higgs. The last process, subject of study in this thesis, is the top Higgs (tH) process. This process is a rare expected process with a very small production rate[6]. In the figure 1.5, is another way to produce tH, in association with a W.
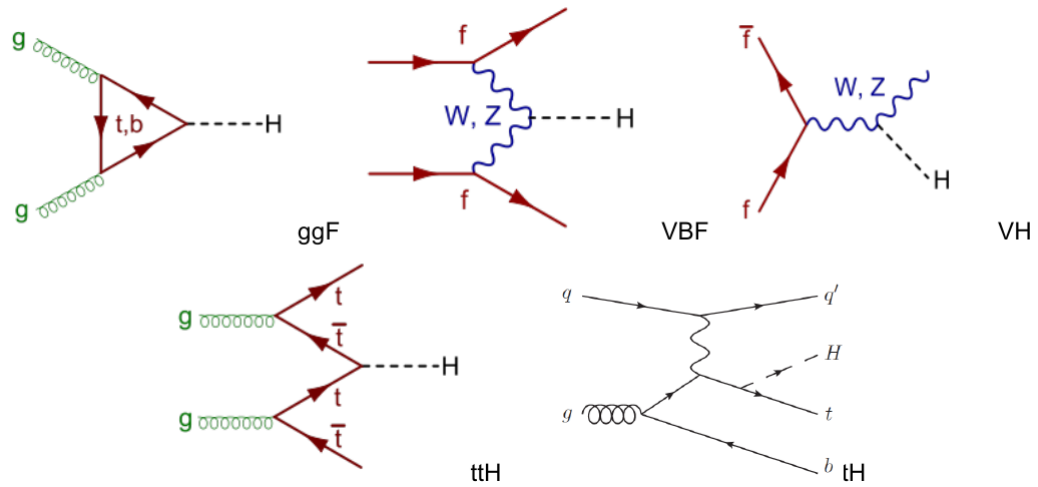
Fig. 1.4 Different Higgs production mechanism, from the most likely to least likely
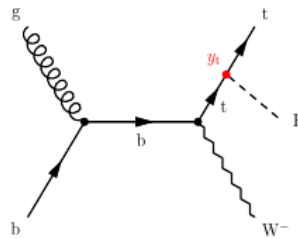
Fig. 1.5 tHW mechanism

171   In tH process, Higgs boson is radiated from a single top quark as shown in 1.4. tH

172 process is a new field of study, given that there are few experiments and its production

173 rate (probability) is small, so the detection of Higgs bosons in this channel opens to new

174 discoveries.

175

176   In particle physics, cross section (σ) describes the likelihood of two particles interacting

177 under certain conditions. Cross sections are expressed in barns , where 1 barn=10^{-34} cm^2 .

178 The cross section is important in the evaluation of events for specific processes. In order to

179 get the number of events for a specific process, the reaction rate N is determined by the

180 total cross section σ and the luminosity L.

181 The unit of measurement of luminosity is cm^{-2}s^{-1}. Therefore, The reaction rate is

$$N_R = \sigma L \tag{1.22}$$

182 In practice, the luminosity is measured by counting the number of events for a well known

183 process.

Table 1.2 Higgs boson production cross sections in pp collisions for $\sqrt{s} = 13$TeV (in pico barn) and number of events for an integrated luminosity of 35.9 fb^{-1} for Run 2 [6]

Production mechanism	σ (picobarns pb)	Number of events
ggF	48.93	1756587
VBF	3.78	135702
WH	1.35	48465
ZH	0.88	31592
$t\bar{t}$H	0.50	18255
tH	0.015	560.39

184   In the table 1.2 shows the Higgs production cross section for pp collision and the number

185 of events produced using a integrated luminosity of 35.9fb^{-1} , that is the luminosity

186 measured for the Run 2 from LHC on 2016[6].

187   Here we can see ggF process have the biggest cross section of all Higgs mechanism

188 and generates the greatest number of events possibles. For the processes tH and $t\bar{t}$H, they

189 have the smallest cross section, so the probability for the processes is low and generates a

190 small number of events.
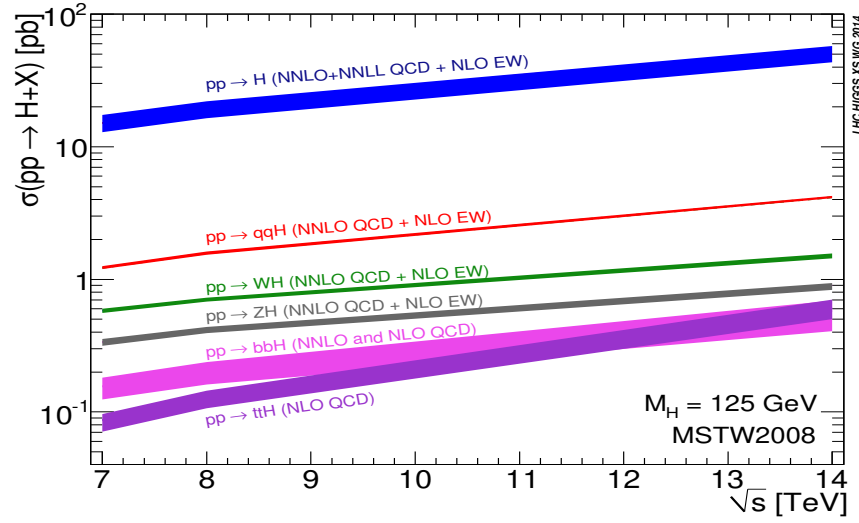
Fig. 1.6 Cross section for different processes generated in a pp collision

1.7 Higgs decay rates

In particle physics, two importatns properties are the lifetime and the decay rates of a particle. The lifetime is related to the total decay rate Γ, that is the probability per unit of time a particle decay,

$$dN = -\Gamma N dt \tag{1.23}$$

with N the original number of particles before the decay. From here is evident that number of particles left in a decay is

$$N(t) = N_0 e^{-\Gamma t} \tag{1.24}$$

The number of particles decreases over time exponentially and this can be measured. With this, it is possible determinate the mean lifetime[7]

$$\tau = \frac{1}{\Gamma} \tag{1.25}$$

In case of the decay rate to a specific process, it is necessary get the branching fraction of the process. The branching ratio for a decay process is the ratio of the number of particles which decay via a specific decay mode with respect to the total number of particles which

decay via all decay modes.

$$BR_i = \frac{\Gamma_i}{\sum_i \Gamma_i} \tag{1.26}$$

Where $\Gamma = \sum_i \Gamma_i$ is the total decay width (sum of all partial widths) of the particle and is related to lifetime of the particle: $\Gamma = 1/\tau$. Since the dimension of Γ is the inverse of time, in our system of natural units, it is measured in inverse seconds,it has the same dimension as mass (or energy)[5] . The lifetime of the Higgs boson is predicted to be 1.56×10^{-22} seconds and corresponds to Γ_H is about 4 MeV , but has not yet been measured due to the detector resolution [3].

The decay $H \to b\bar{b}$ have a branching ratio a bit more than 50%, therefore is the most

Table 1.3 SM Higgs boson branching ratios for M_H =125 GeV [6]

Higgs decay	Branching ratio (BR)
$H \to b\bar{b}$	58.4%
$H \to W^+W^-$	21.4%
$H \to \tau^+\tau^-$	6.27%
$H \to ZZ$	2.62%
$H \to \gamma\gamma$	0.227%
$H \to Z\gamma$	0.153%
$H \to \mu^+\mu^-$	0.0218%

likely decay Higgs boson can decay. Due to this, $H \to b\bar{b}$ is a very studied process and most likely to detect a Higgs boson in the data after reconstruction. The decay $H \to \mu^+\mu^-$ has a very low branching ratio. This decay is very rare but not imposible to detect in the future. In this work the majority of the Higgs decays detected are from WW, ZZ, $\tau\tau$

1.8 *tH* production mechanism

The production of *tH*, where a Higgs boson can be radiated either from the top quark or from the exchanged W boson in the two dominant leading order diagrams in figure 1.7 provides a unique opportunity to study the relative sign of the coupling. In SM , the two diagrams interfere negatively and thereby suppress the production cross section. Any deviation from the SM can lead to a large enhancement of the event rate. κ_t and κ_V are the coupling parameters, where κ_t is for the top and κ_V for W boson.

---

[5]Cleaves H.J. (2011) Branching Ratio. In: Gargaud M. et al. (eds) Encyclopedia of Astrobiology. Springer, Berlin, Heidelberg
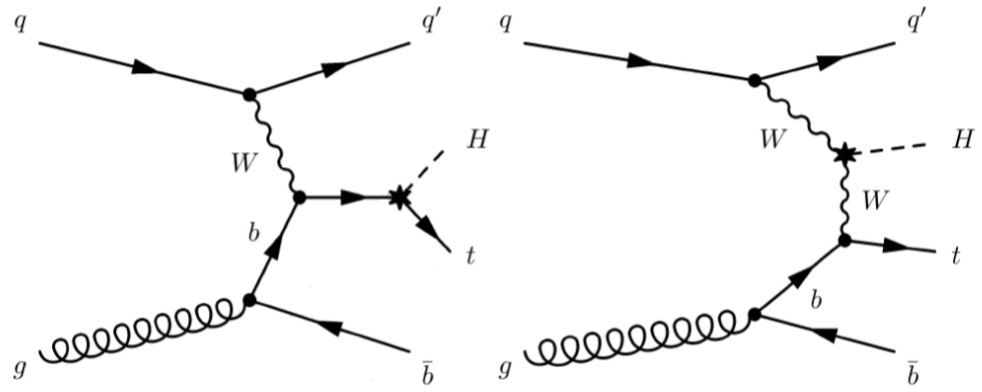
Fig. 1.7 tH mechanism. Higgs radiated from a top quark (left). Higgs radiated from a W boson (right) [1]

Chapter 2

The LHC and CMS

2.1 The Large Hadron Collider

The Large Hadron Collider (LHC) is one the largest and most powerful particle accelerator in the world. It came on operation on 10 September 2008 and it is the most recent addition from the European Organization for Nuclear Research (CERN). The LHC is a 27 kilometer ring composed of superconducting magnets with accelerating structures to boost the energy of the particles.

The LHC is designed to accelerate particles to high energies and generate collisions. There are several experiments installed along the LHC ring. One of them is ATLAS, located on Point 1 between the two injection lines , which is a general purpose detector. At point 5 is another general purpose detector: the compact muon solenoid (CMS). A particle detector optimized for heavy ion physics, ALICE, is located at Point 2 and LHCb, a detector designed for B physics, is located at Point 7.[14, 15]

Inside the accelerator, two high energy particles beams travel at close to the speed of light before they collide. In order to make them collide, beams travel in opposite directions in separate beam pipes, two tubes kept at ultrahigh vacuum. By using of superconducting electromagnets that generates a powerful magnetic field , the beams are guided around the accelerator ring. The electromagnets are built from coils of special electric cable that operates in a superconducting state, efficiently conducting electricity without resistance or loss of energy.For that, it is required to have magnets to a temperature of -271.3 C. To reach such temperatures, a system of liquid helium is connected to the accelerator.[15]
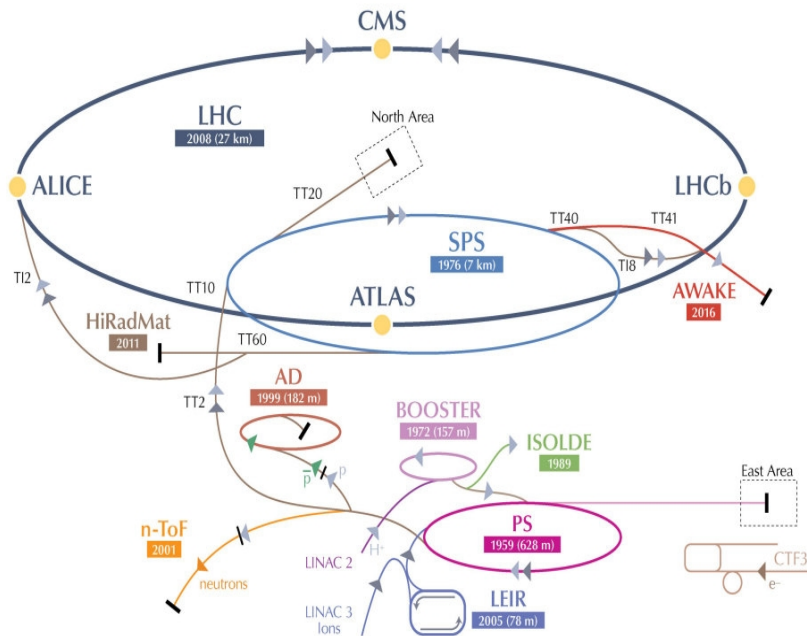
Fig. 2.1 Large hadron collider from CERN

Protons in the LHC start out as hydrogen atoms stripped of their electrons. The first accelerating stage the protons are subjected to is a linear accelerator, Linac2, which accelerates them up to 50 MeV . The protons are then sent into the Proton Synchotron Booster which accelerates them up to 1.4 GeV before sending them to the Proton Synchotron (PS). The protons leave the PS at 25 GeV before entering the Super Proton Synchotron (SPS), which accelerates them to the LHC injection energy of 450 GeV. After this stage, the beam is ready to be injected into the LHC through one of two injection lines with 6.5 TeV.[2]

Table 2.1 Accelerator operation energies

Accelerator	Energy
Linac 2	50 MeV
PS Booster	1.4 GeV
Proton Scyncroton (PS)	25 GeV
SPS	450 GeV
LHC	6.5 TeV

242   Inside the detectors, collided protons generates an amount of particles such as pion and
243 kaons, which are the most commons, created by the jet particles that were created after
244 the collision. Besides of the particles created by the quarks of the proton , gluons are also
245 radiated and create new particles and photons are radiated too.
246 During the collision time, the main detectors of LHC capture the energy and save the data
247 in supercomputers. Those high end computers starts to measure the signals in order to
248 assign a type of events.
249

250   The main objetive of the LHC is to study the nature of electroweak symmetry breaking
251 for the Higgs mechanism of the SM. Alternatives to the Standard Model that involves
252 different symmetries are also put on test. With the exploration of theses theories, people
253 hope for a discovery that guide them toward a unified theory, so the importance to accelerate
254 particles to higher energy scales.
255 The LHC has a schedule where there is a period of experiments that last for three or four
256 years. Ending the experimental time, the engineers of the LHC start the maintenance.
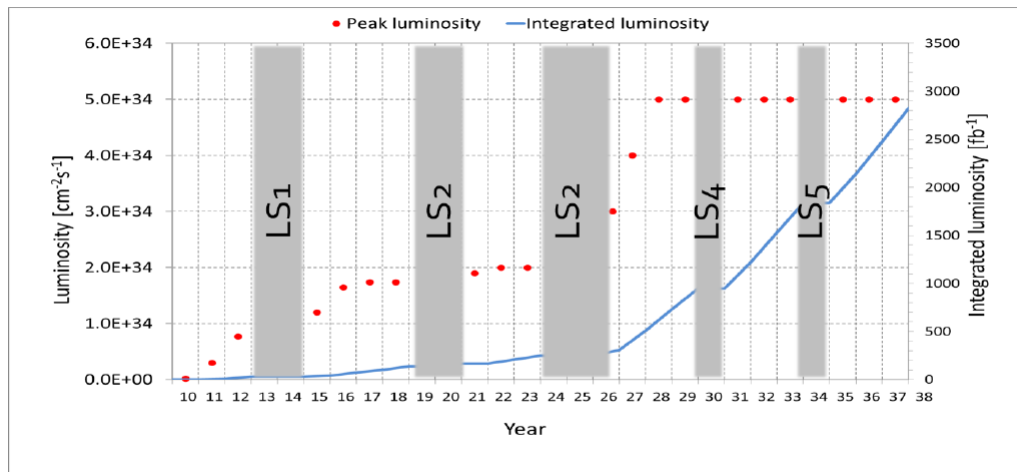
Fig. 2.2 LHC schedule, including future plans for increase the center of mass energy and
luminosity. The periods labeled LS are the maintenance periods [2].

257   From the figure 2.2, shows the Large Hadron Collider forecast for the increase of
258 luminosity for the next years. Red dots are peak luminosity expected to reach and blue line
259 is integrated luminosity. In the year 2018, the maximum integrated luminosity is around
260 150 fb^{-1}[2]. From 2019 to 2021 the second phase of maintenance, where engineers
261 increase the performance of the accelerator, give maintenance to the system and introduce
262 new components to the complex. After that period, the LHC starts new collision period at
263 even higher energies in order to explore new particle phenomena.

2.2   The Compact Muon Solenoid

The Compact Muon Solenoid (CMS) is a detector with multiple uses in the LHC and part of the main experiments at CERN. Located underground in the France- Switzerland border , in the city of Cessy, France. This detector was designed in the early 1990s, based on the mass limit of the Higgs boson, and put on operation in 2008, it has a big solenoid that generates a great magnetic field of 4 teslas with the objective to separate particles after a particle collision. The detector is 21 metres long, 15 meters wide, 15 meters high ,it has a diameter of 5.9 m with a weight of 12000 ton. The reason for such a strong magnetic field is to obtain a better momentum resolution . The magnetic flux is returned via a 1.5 m thick iron yoke instrumented with four stations of muon chambers.
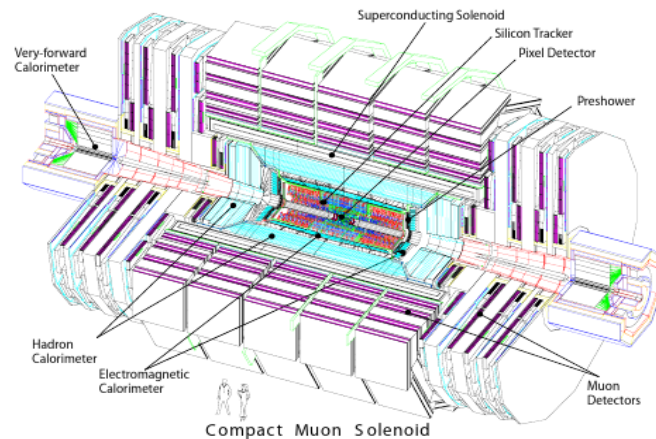
Fig. 2.3 View of Compact muon solenoid (CMS)

There are many layers of detectors to register different kinds of energy signals. But since muons go through materials very easy, the complex is buried 100 meters underground.

The CMS experiment is composed of several detector layers that allow identify and save different types of energy signals and it is saved in a powerful supercomputers that separate and classify the data according to certains variables. The general parts of the CMS are the Silicon Tracker , an Electromagnetic Calorimeter,a Hadron Calorimeter, the solenoid (superconducting magnet) and the Muon Detector.

The objectives of the CMS experiment are numerous. One of them is identification of muons by measuring the momenta and scattering angle. Muons can be produced in interesting events like Higgs, $W^{\pm}$ and Z boson decays.This experiment along the ATLAS experiment discovered the Higgs boson in 2012.

Table 2.2 Characteristic of the CMS superconducting solenoid [3]

Field strength	4 T
Inner Bore	5.9 m
Length	12.9 m
Number of Turns	2168
Current	19.5 kA
Stored energy	2.7 GJ

2.2.1   Silicon Tracker

The Silicon Tracker is the first of the main subdetectors of CMS from inside to outside. The Tracker is composed of two sub components: Pixel and Strip detectors.The outer radius of the tracker is 110 cm, and its total length is 540 cm. The tracker coverage is $|\eta| < 2.4$[1].

In the Pixel barrel section, there are 3 layers of pixel sensors with radii of 4.4, 7.3 and 10.2 cm with a length of 53 cm. Each pixel has an area of 100×150 μm^2. The barrel section has 768 pixel modules. The Pixel endcap has 2 disks on each side placed at 34.6 and 46.5 cm in the z axis. Each disk covers radii from 6 to 15 cm and is divided into 24 blades with 7 modules each blade. They are assembled in a turbine-like geometry that contains a total of 672 pixel modules.

The Strip Detector is divided in 4 sections: Tracker inner barrel (TIB), tracker outer barrel (TOB), tracker encap (TEC) and tracker inner disk (TID). The region that cover the barrel section is $|z| < 65$ cm for TIB and $|z| < 110$cm for TOB.The first two are composed of silicon sensors layers of 4 and 6 layers respectively. The TEC has 9 disk extending in the region 120 cm > $|z|$ > 280 cm .The TID comprises 3 small disks that fill the gap between the TIB and the TEC.

The Strip Detector have almost 15 400 modules, mounted on carbon-fibre structures and housed inside by a temperature controlled outer support tube. The operating temperature must be around -20°C. The total area of the pixel detector is around 1 m^2 and the silicon strips is 200 m^2. The inner tracker comprises 66 million pixels and 9.6 million silicon strips [3]. A full coverage of the Tracker is shown in figure 2.4

During the particle collision, it generates a lot of different particles that pass first through the inner tracker, interacting with the sensors layers and registering the particle path. By reconstructing the path of the particles, it is possible to generate a track, which allows to measure the momentum of the particle by calculating its curvature. The tracker is

---

[1]η , called pseudorapidity, is a coordinate where $\eta = -\ln\tan\frac{\theta}{2}$
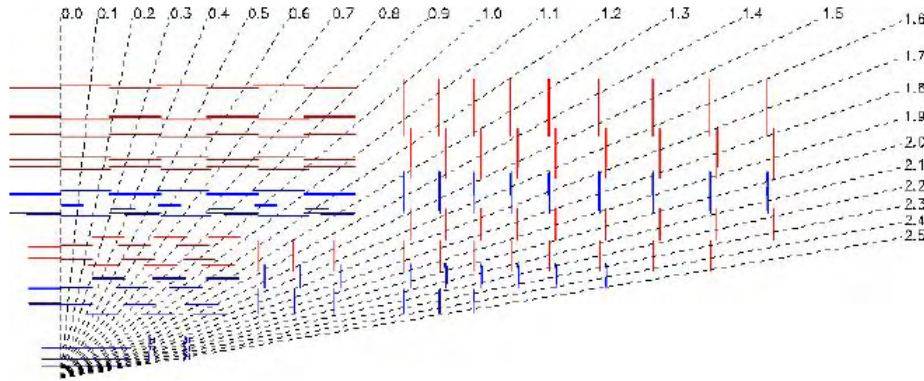
Fig. 2.4 The Tracker layout distributed in terms of η.

used to reconstruct the path of charged particles (e.g. electrons, muons, pions). The most important objects of study are the momentum and the vertex (origin of the track). The efficiency of the tracker is estimated by using samples of muons and pions with p_t of 1,10 and 100 GeV. For muons the efficiency of the tracker is shown in 2.5
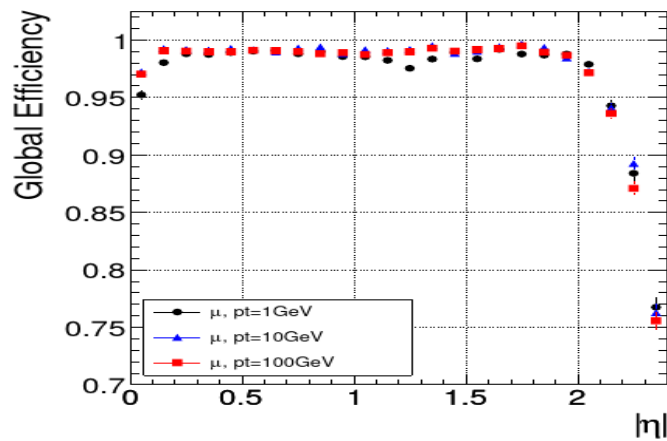
Fig. 2.5 Total reconstruction efficiency for muons

According to figure 2.5, the efficiency of the tracker is around 98 % for $|\eta| < 2$. The resolution of the tracker for muons with p_t=100 GeV is around 1-2 %.
Of course, this is a first stage of the measurement of particle momentum because the other detectors are used to increase and improve the measurement and reconstruction of the particle path.

2.2.2 Electromagnetic calorimeter

The electromagnetic calorimeter or ECAL is a calorimeter composed of 61200 lead tungstate ($PbWO_4$) crystals that act as scintillanting crystals (emits light when particles interact with the crystal). These calorimeters are mounted in the central barrel and closed

by 7324 crystals in the both endcaps. The barrel section of the ECAL covers the range $|\eta| < 1.479$. The crystals in the barrel have a pyramid shape and their crosss section is 22×22 mm^2 at the front face and 26×26 mm^2 at rear face. The crystal length is 230 mm.The EB (barrel section of ECAL) has a inner radius of 129 cm[3]

The endcaps cover have the range $1.479 < |\eta| < 3.0$. The distance between the interaction point and the endcap is 3.144 m. The endcap has identically shaped crystals grouped in mechanical units of 5×5 crystals. The crystal cross section for the rear face is 30×30 mm^2 ,and for front face cross section is 28.62×28.62 mm^2 with length of 220 mm.
 In the barrel, there photo detectors called avalanche photo diodes (APD), made of silicon
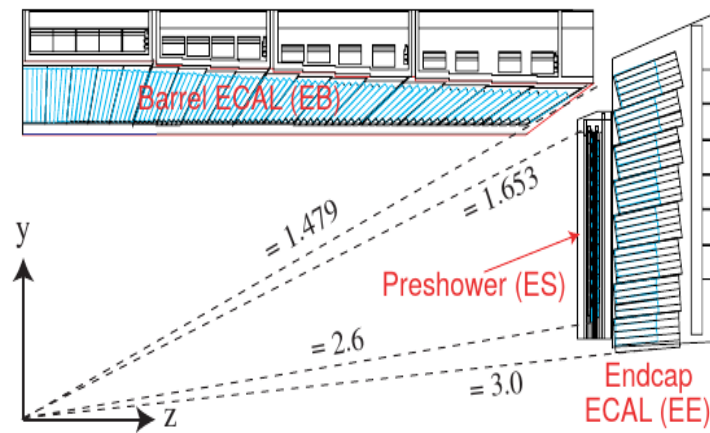
Fig. 2.6 View of the ECAL

with a active area of 5×5 mm^2 with 2 glued to the back of each crystal. At the endcap , the photo detectors are vacuum photo diodes (VPT), made of with an anode of copper mesh (10 μm) , allowing to operate in the magnetic field. VPT have a size of 25 mm in diameter , glued to the back of each crystal.

There is also a preshower detector , which principal function is to identify neutral pions in the endcaps within the region $1.653 < |\eta| < 2.6$. It also helps the identification of electrons against minimum ionizing particles, and improves the position determination of electrons and photons.

As its name says, the ECAL is mainly used for the electron detection, but also detects, photons, and neutral pions. The charged particles reach the crystals that provokes the photo diodes detect energy.
The resolution of the ECAL is estimated by using a test beam and registering the energy signals. The resolution for electrons with energies of 120 GeV, it has obtained a resolution of 0.5%.

2.2.3   Hadron calorimeter

The hadron calorimeter (HCAL) along the ECAL, form a complete calorimeter that allows to measure the jets and missing transverse energy. HCAL is located in the barrel and the endcaps, surrounding the ECAL and affected by the magnetic field generated by the solenoid. The Barrel section (HB) and endcap section (HE) cover the pseudorapity $0 < |\eta| < 1.3$ and $1.3 < |\eta| < 3.0$ respectively.

The HB is an assembly of two half barrels, composed of 18 wedges.Each wedge has 17 active layers composed of scintillator tiles with 16 layers of absorber metal (brass and stainless steel).Each tile has a size of $\Delta\eta\Delta\phi = 0.087 \times 0.087$. Light of scintillator is collected by a single wave length shifting fiber (WLS) for each scintillator tile. The wedge has a inner radius of 1777 mm to an outer radius of 2876.5 mm.

HE is composed by brass absorber plates ,with the thickness of 78 mm, and a total of 19 scintillator layers with a thickness of 3.7 mm. HE is sectioned in 5 in ϕ to match the barrel wedges. .

The outer barrel hadron calorimeter (HO) consists of layers of scintillator with thickness
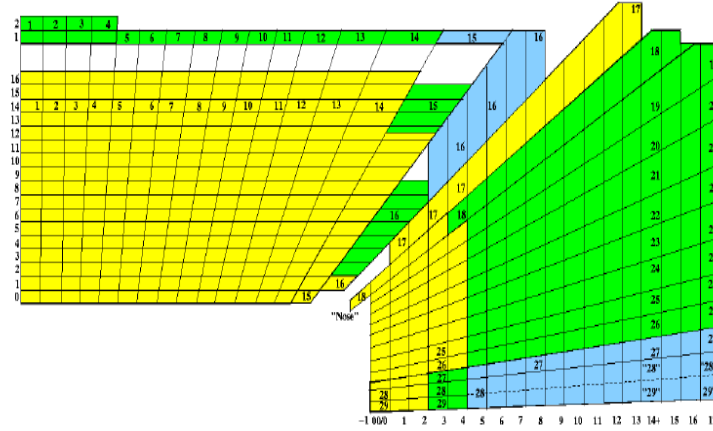
Fig. 2.7 View of the CMS HCAL showing the different layers and tower regions. In the endcap, the towers are defined with two longitudinal segments as shown by the colors

of 10 mm, located outside of the magnet coil that cover the region $-1.26 < |\eta| < 1.26$. There is also a foward calorimeter (HF) located at 11.2 m from the interaction point, that cover the region of $2.9 < |\eta| < 5$. They are made of steel absorbers and embedded radiation hard quartz fibers,which collects Cherenkov light[3].

The tiles are arranged in a tower pattern in the $\eta - \phi$ space, projective to the inter-action point. In total there are 4176 towers. The towers are used as input to several jet reconstruction algorithms.

381   The HCAL measures the energy of hadrons,such as the pions and kaons. The energy
382 resolution of the HCAL was estimated using a test beam of pions. For 100 GeV pions, the
383 resolution obtained is 12%.

388

2.2.4   Muon Detector

385 The Muon Detector has three main subdetectors: the drift tubes chambers (DT), the cathode
386 strips chambers (CSC) and the resistive plate chamber (RPC). The DT's, CSC's and RPC's
387 are shown in the figure 2.8.

388

389   The DT chambers cover the barrel section $|\eta| < 1.2$, composed of rectangular gas filled
390 active cells. Those cells have a transverse size of 42×13 mm^2 with a 50 μm diameter
391 anode wire at the center that operates at voltages of over 3600 V. The gas used in this cells
392 is a mix of Ar and CO_2 with a proportion of 85 % and 15 %. There are 250 chambers in 4
393 layers inside the magnet return yoke, with radii of approximately 4.0, 4.9, 5.9 and 7.0 m
394 from the beam axis and 12 sections covering $30°$ in ϕ each one.
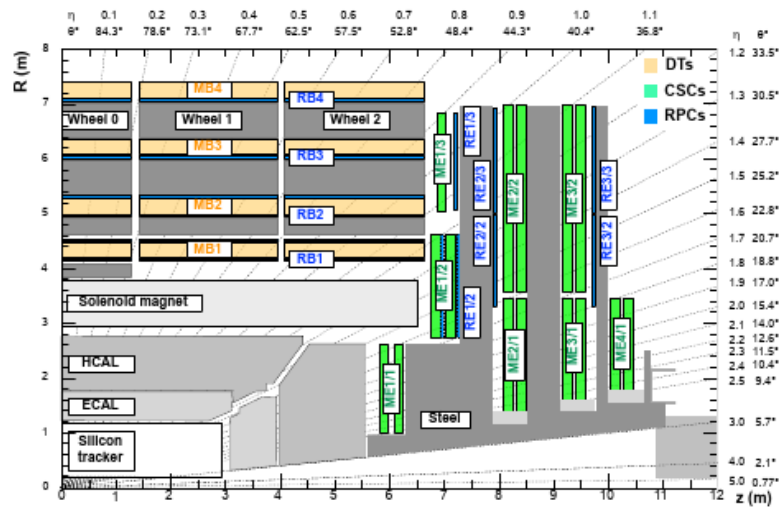
Fig. 2.8 Cross section of a quadrant of the CMS with axis parallel to the beam (z axis)
horizontally and the radius of the detector in terms of the η.

395

396   The CSC's are located in the endcap regions $0.9 < |\eta| < 2.4$. The CSC's are installed
397 on the face of steel disks perpendicular to the beam. Each CSC has a trapezoidal shape
398 and consist of 6 gas gaps between 7 metal plates, where each gap contains copper cathode
399 strips and anode wires running almost perpendicularly to the strips, with a diameter of 50
400 μm separated by 3.16 mm. The chambers use a gas mixture of 50% CO_2 , 40 % Ar and
401 10% CF_4. The muon endcap system comprises 468 CSCs in the 2 endcaps [3, 16].

402
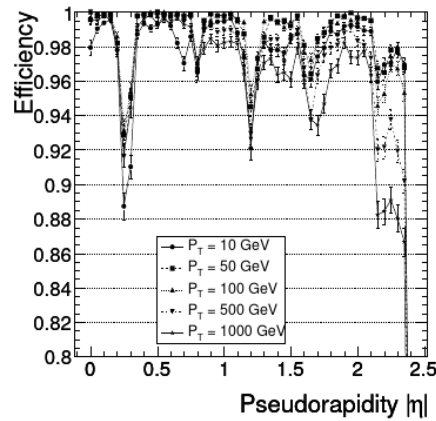
Fig. 2.9 Muon reconstruction efficiency in terms of η and p_t [3]

The RPC are located in the barrel and endcap regions that covers the range o $|\eta| < 1.6$. The main purpose is to trigger events with muons. RPC's are structured with a double gas filled gap and readout strips between the gaps .

The gas mix used in the RPC consist of 95.2% Freon ($C_2H_2F_4$), 4.5% isobutane (C_4H_{10}), and 0.3% sulphur hexafluoride (SF$_6$)[16].

The main purpose of the Muon System Detector is to identify muon tracks. The efficiency of the muon system is estimated by using single muon samples simulated with p_t=10, 50, 100, 500 and 1000 GeV. The results are shown in the figure 2.9. The graph shows an efficiency of approximately 98% in the the fully instrumented regions. In the intersection regions, there are drops in efficiency due to the separation of the chambers.

Chapter 3

Event reconstruction and selection

During the proton collision, many types of processes happen whose information are saved in the CMS data storage system. But the events are only saved if they fulfill certain conditions compatible with the signal. For the tH process , the search is based on the presence of a pair of muons with the same sign. The rest of the processes that also generates a pair of muons with the same sign will be considered backgrounds.

3.1 Signal Event Topology

In this search, top quark decays to Wb and from the W boson decays to a muon and a neutrino. The Higgs decays to a pair of opposite sign W bosons, where one of the bosons can decay to a μ and its neutrino. This is the main process that generates events with two same sign muons.The tH process topology is shown in the figure 3.1.

Figure 3.1, also shows a b-jet that comes from the tH process. Finally there is a forward quark jet (highest η value) generated from the initial collision. Additional jets or leptons can be generated from the other W boson.

Due to the small cross section of the tH process, the amount of tH events is low compared to other Higgs production processes. Table 3.1 shows several processes that generate same sign muon events for tH. These numbers do not consider the detection efficiency.

Fig. 3.1 Topology of tH process which generates two same sign muons , a forward jet and a b-jet.

3.2   Backgrounds

Several processes contribute to the background in this search:

- $t\bar{t}W^{\pm}$ and $t\bar{t}Z$ ($t\bar{t}V$): One muons comes from a top and the other comes from the vector boson.

- W^+Z: Diboson production with leptonic decays. One muon comes from W boson and the other from Z boson.

- $W^{\pm}W^{\pm}$:A pair of same sign W bosons generate a muon each one.

- tZq: Processes with single top quarks associated with a Z boson, where $Z \to \mu^+\mu^-$, also contribute to the background.

- $t\bar{t}t\bar{t}$:In these type of events, one t decays to Wb and W decays to a muon. The second muon comes from the other top decay.

- W^+W^-Z, ZZZ and W^+ZZ (VVV): The leptonic decays of the W or Z bosons generate at least two same sign muons.

- tZW^+:One muon comes from the Z while the other same sign muon can come from t or W.

- **ZZ**: Each muon comes from Z boson decays.

- **$t\bar{t}H$**: This Higgs production mechanism is considered a background in this analysis. The muons in this cases comes from one top and Higgs decays.

- **Fakes**:This background refers to events where two muons come from b meson decays in jets.

Table 3.2 show the decay chains and production cross section for background. Due to small expected event yields, the processes $W^{\pm}W^{\pm}$,tZq,$t\bar{t}t\bar{t}$ VVV, tZW^{+} and ZZ are grouped as one called Rares in the results below.

Table 3.1 Expected number of events for different tH decay chains assuming integrated luminosity of 35.9 fb^{-1}. l represents $\mu^{\pm}, e^{\pm}, \tau^{\pm}$.

Decay chain	BR	Events
$tH \rightarrow W^+bW^+W^- \rightarrow \mu^+ \nu_\mu b \mu^+ \nu_\mu q\bar{q}'$	2.096×10^{-3}	1.173
$tH \rightarrow W^+bW^+ W^- \rightarrow \mu^+\nu_\mu b \mu^+\nu_\mu l^- \bar{\nu}_l$	3.37×10^{-4}	0.899
$tH \rightarrow W^+b \tau^+\tau^- \rightarrow \mu^+\nu_\mu b \mu^+\nu_\mu \bar{\nu}_\tau l^- \bar{\nu}_l \nu_\tau$	3.637×10^{-4}	0.203
$tH \rightarrow W^+b W^+W^- \rightarrow \tau^+\bar{\nu}_\tau b \mu^+\nu_\mu q\bar{q} \rightarrow \mu^+\nu_\mu \bar{\nu}_\tau \bar{\nu}_\tau b\mu^+\nu_\mu q\bar{q}$	1.890×10^{-4}	0.105
$tH \rightarrow W^+b\tau^+\tau^- \rightarrow \mu^+ \nu_\mu b \nu_\tau \mu^+ \nu_\mu \bar{\nu}_\tau q\bar{q}$	1.681×10^{-4}	0.094
$tH \rightarrow W^+b W^+W^- \rightarrow \tau^+\bar{\nu}_\tau b\mu^+\nu_\mu l^- \bar{\nu}_l \rightarrow \mu^+\nu_\mu \bar{\nu}_\tau \bar{\nu}_\tau b\mu^+\nu_\mu l^- \bar{\nu}_l$	3.045×10^{-5}	0.017
$tH \rightarrow W^+bZZ \rightarrow q\bar{q}bZZ \rightarrow q\bar{q}b\mu^+\mu^-\mu^+\mu^-$	1.966×10^{-5}	0.011
$tH \rightarrow W^+b \tau^+\tau^- \rightarrow \tau^+\bar{\nu}_\tau b \mu^+\nu_\mu\bar{\nu}_\tau q\bar{q}'\nu_\tau \rightarrow \mu^+\nu_\mu\bar{\nu}_\tau\bar{\nu}_\tau b\mu^+\nu_\mu\bar{\nu}_\tau q\bar{q}'\nu_\tau$	1.549×10^{-5}	0.008

Table 3.2 Main backgrounds and their same sign $\mu\mu$ decay process

Background	Decay process
$t\bar{t}W$	$t\bar{t}W \rightarrow W^+bW^-\bar{b} \mu^+\nu_\mu \rightarrow \mu^+\nu_\mu b \mu^- \bar{\nu}_\mu\bar{b} \mu^+\nu_\mu$
$t\bar{t}Z$	$t\bar{t}Z \rightarrow W^+b W^-\bar{b}\mu^+\mu^- \rightarrow \mu^+\nu_\mu b \mu^- \bar{\nu}_\mu\bar{b}\mu^+\mu^-$
W^+Z	$W^+Z \rightarrow \mu^+\nu_\mu\mu^+\mu^-$
$W^\pm W^\pm$	$W^+W^+ \rightarrow \mu^+\nu_\mu\mu^+\nu_\mu$
tZq	$tZq \rightarrow W^+ b\mu^+\mu^- q \rightarrow \mu^+\nu_\mu b \mu^+\mu^- q$
$t\bar{t}t\bar{t}$	$t\bar{t}t\bar{t} \rightarrow W^+b W^-\bar{b} W^+b W^-\bar{b} \rightarrow \mu^+\nu_\mu b \mu^- \bar{\nu}_\mu\bar{b} \mu^+\nu_\mu b \mu^- \bar{\nu}_\mu\bar{b}$
W^+W^-Z	$W^+W^- Z \rightarrow \mu^+\nu_\mu \mu^- \bar{\nu}_\mu\mu^+\mu^-$
ZZZ	$ZZZ \rightarrow \mu^+\mu^-\mu^+\mu^-l^+l^-$
W^+ZZ	$W^+ZZ \rightarrow \mu^+\nu_\mu\mu^+\mu^-l^+l^-$
tZW^+	$tZW^+ \rightarrow W^+b\mu^+\mu^-\mu^+\nu_\mu \rightarrow \mu^+\nu_\mu b\mu^+\mu^-\mu^+\nu_\mu$
ZZ	$ZZ \rightarrow \mu^+\mu^-\mu^+\mu^-$
$t\bar{t}H$	$t\bar{t}H \rightarrow W^+bW^-\bar{b}W^+W^- \rightarrow \mu^+\nu_\mu b\mu^- \bar{\nu}_\mu\bar{b} \mu^+\nu_\mu \mu^- \bar{\nu}_\mu$

3.3   Event Selection

In order to detect signal events and reject background, the following selections are applied.

- The events must contain two muons with the same sign.

- Transverse moment $p_t > 25$ GeV for the highest p_t muon and $p_t > 15$ GeV for the lowest p_t muon.

- A forward jet with $p_t > 40$ GeV and $|\eta| > 2.4$

- One or more b-tagged jets with $|\eta| < 2.4$

The number of events that passed the event selection are shown in table 3.3 which corresponds to a integrated luminosity of 35.9 fb^{-1} [11]. The backgrounds with the most events are $t\bar{t}W^{\pm}$, $t\bar{t}Z$ and Fakes. For the SM signal tH, the number of expected events is 2.14, while for the inverted coupling scenario ($k_t = -1$) the cross section is enhanced by a factor of approximately 10. This event yields will be used to estimate the signal sensitivity.The yields include statitical uncertanties due to the simulated samples and systematic uncertanties are described below.

Table 3.3 Event yields for signal and backgrounds after the event selection for a integrated luminosity of 35.9 fb^{-1}. The uncertainties of yields include statistical and systematic

Process	Number of events
$t\bar{t}W$	68 ± 10
$t\bar{t}Z$	25.9 ± 3.9
WZ	15.1 ± 7.7
Rares	20.9 ± 4.9
Fakes	80.9 ± 9.4
$t\bar{t}H$	24.2 ± 2.1
tH (SM)	2.14 ± 0.13
tH ($k_t = -1$)	26.2 ± 2.2

3.4   Systematic uncertanties

The uncertainties on $t\bar{t}W$ and $t\bar{t}Z$ event yields are mainly due to the uncertainties of their production cross sections. The uncertainty on WZ background is estimated using real data events in a three lepton control region. In the Rare backgrounds, which are not measured, a 50% of uncertainty is assigned. The uncertainty on the Fakes background is estimated using real data in a control region, defined by the muon identification criteria. For the Higgs processes tH and ttH , the uncertainty are due to the theoretical parameters used in that simulation.

3.5   Multivariable discriminant

Due to small signal to background ratio caused by the small cross section of tH, a multivariable discriminat, which separates signal from backgrounds, is necessary to optimize the signal sensitivity. The multivariable discriminant is a Boosted Decision Tree (BDT) that takes a set of input features and splits input data recursively based on those features. The features can be a mix of categorical and continuous data. The BDT training is performed using several event variables.

In this analysis, the BDT discriminant was trained to discriminate against $t\bar{t}V$ background, because this background is one of the largest backgrounds. The variables used for the BDT were the following:

- Number of jets with pT > 25 GeV, $|\eta| < 2.4$

- Maximum $|\eta|$ of forward jet

- Sum of lepton charges

- Number of jets with $|\eta| > 1.0$

- $\Delta\eta$ between forward jet and b-jet with highest p_t

- $\Delta\eta$ between forward jet and b-jet with lower p_t

- $\Delta\eta$ between forward jet and closest muon

- $\Delta\phi$ of highest p_t same-sign muon pair

- min ΔR (muon pairs)[1]

- p_t of muon with lower momentum

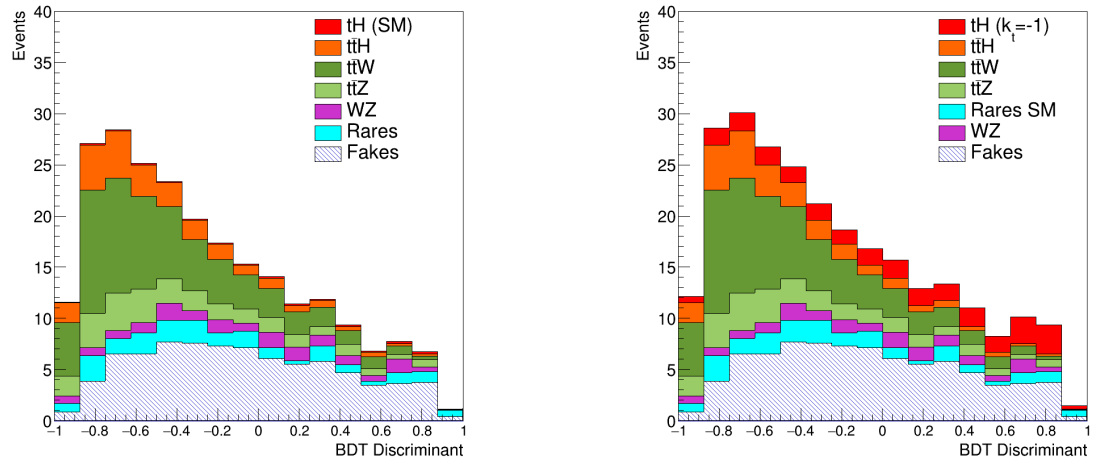[1] $\Delta R = \sqrt{\Delta\eta^2 + \Delta\phi^2}$, where ΔR is the distance in the $\eta\phi$ plane

Fig. 3.2 Distribution of BDT discriminant for signal and background in the case of SM (left) and inverted coupling scenario (right)

Chapter 4

Statistical Analysis

To estimate the sensibility of the *tH* signal, we define an Asimov dataset, made by replacing the ensemble of simulated backgrounds and signal by a single one. The statistical uncertainty of the Asimov data is calculated as $\sqrt{n}$, with n the number of events. The uncertainty of the signal strength is estimated by applying a fit to the Asimov dataset, where the model is constructed from the sum of the individual backgrounds and signal. The fit is implemented using a Poisson likelihood and gaussian constraints for the systematical uncertainties in the model.

4.1 Likelihood and fit procedure

The likelihood function is the product of Poisson probabilities for all bins of the BDT distribution. The likelihood function has the form

$$L(\mu, \alpha) = \prod_{j=1}^{N} \frac{(\mu s_j + b_j)^{n_j}}{n_j!} e^{-(\mu s_j + b_j)} \prod_{k=1}^{M} e^{\frac{-\alpha_k^2}{2}} \tag{4.1}$$

where N is the total number of bins, n_j is the number of events in a bin j, s_j is the number of signal events, μ is a parameter that modifies the signal strength and b_j is the number of background events. b_j is the sum of different background processes k

$$b_j = \sum_k b_j^k (1 + \alpha_k \sigma_k) \tag{4.2}$$

α_k is the parameter that modifies the expected background prediction and σ_k is the systematic uncertainty of the associated background. σ_k for signal and backgrounds are shown in

₄₂₄ the table 3.3

₄₂₅

₄₂₆   The fit is applied by minimizing the $-\log L$ (NLL) with respect to the parameter μ and
₄₂₇ α_k. The minimization is performed by using the package ROOFIT [17].

Table 4.1 Postfit yields for the fit to the Asimov data corresponding to 35.9 /fb. The
uncertainty given is the combined statistical plus systematic.

Process	SM	$k_t = -1$
$t\bar{t}W$	68±8.9	68 ±8.9
$t\bar{t}Z$	25.9±3.8	25.9±3.8
WZ	15.1±7.4	15.1±7.4
Rares	20.8±4.8	20.8±4.8
Fakes	80.9±9.0	80.9±8.9
$t\bar{t}H$	24.2±2.0	24.2±2.0
tH	2.1±16.5	26.2±13.1

₄₂₈   In the figure 4.1 and table 4.1 , shows the results of the model fitting using the Asimov
₄₂₉ data for both models. As mentioned before, the $k_t = -1$, the number of events for the tH
₄₃₀ signal is more than ten times, compared to SM. This improves the sensitivity to the signal.
₄₃₁ Due to the small number of signal events the uncertainty for the SM is large compared to
₄₃₂ the k_t=-1 scenario, where the uncertainty is around 50%. In this analysis only the signal is
₄₃₃ affected by the change k_t=1 (SM) $\rightarrow k_t = -1$, therefore the backgrounds remain the same.
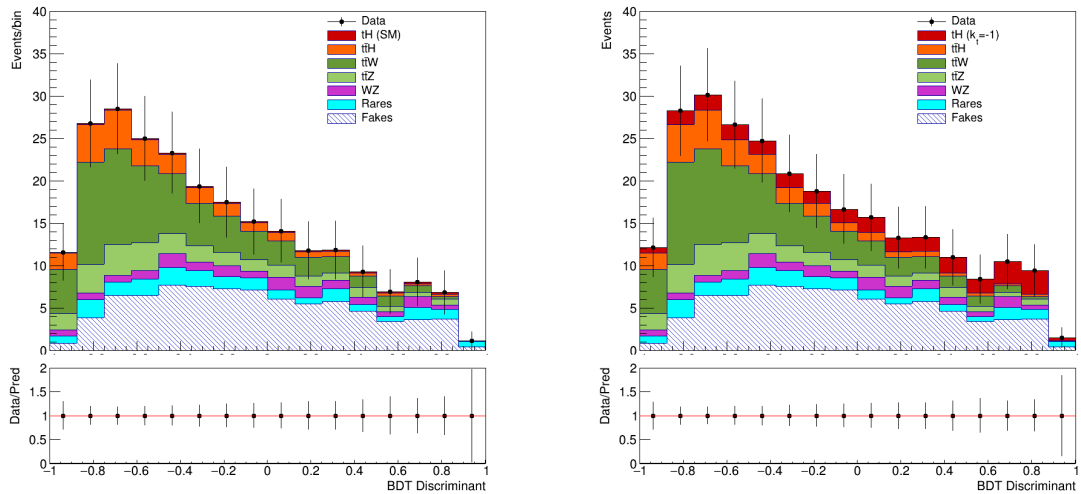In the table 4.2, shows the μ and α parameters. For the pre-fit, values of α are set to zero

Fig. 4.1 Post fit signal and background yields for tH process for SM (Left) and $k_t = -1$
(Right). In the box below each distribution, the ratio of the observed and predicted event
yields is shown

₄₃₄

₄₃₅ and μ is set to 1.After the fit, α parameters set to zero indicates that in the fit, the values of

the backgrounds didn't changed for the SM and the μ parameter set to 1 indicates that the signal strength also didn't changed.

Table 4.2 α and μ values for the fit to Asimov data corresponding to 35.9 fb $^{-1}$

Parameter	SM	kt
μ	1.00 ± 7.74	1.0 ± 0.5
$\alpha_{t\bar{t}W}$	0.00 ± 0.89	0.00 ± 089
$\alpha_{t\bar{t}Z}$	0.00 ± 0.98	0.00 ± 0.98
α_{WZ}	0.00 ± 0.97	0.00 ± 0.97
α_{Rares}	0.00 ± 0.95	0.00 ± 0.98
α_{Fakes}	0.00 ± 0.96	0.00 ± 0.95
$\alpha_{t\bar{t}H}$	0.00 ± 0.98	0.00 ± 0.98

4.2   Limit calculation

Due to the large background, the signal strength for the Asimov data with 35.9 fb^{-1} is consistent with zero. Therefore, we estimate an upper limit on the signal strength at 95% confidence level.

We can define the likelihood ratio

$$\lambda(\mu, \alpha) = \frac{L(\mu, \alpha)}{L(\hat{\mu}, \hat{\alpha})} \tag{4.3}$$

Where $\hat{\alpha}$ and $\hat{\mu}$ are the parameters obtained in the previous section which correspond to the minimal of the NLL. To determine an upper limit on the strength parameter μ , we use the following statistical test

$$q = -2 \ln \lambda(\mu) \tag{4.4}$$

High values of q represent greater incompatibility between the data and the fit model. q is a random variable with a χ^2 distribution [18].

In order to find the upper limit value of μ, we search for the largest value of μ such that q remains below the shaded region shown in 4.2, where α=0.05 in this case. It is useful to scan q as function of μ , which is normally a parabolic function as shown in 4.3.In the SM case, the scan has a wider shape in comparison to the k_t=-1. This is due to larger statistical uncertainty on the μ parameter. Using the above technique, we find an expected upper limit $\mu <17.0$ for SM model and $\mu < 2.3$ for k_t=-1 model.
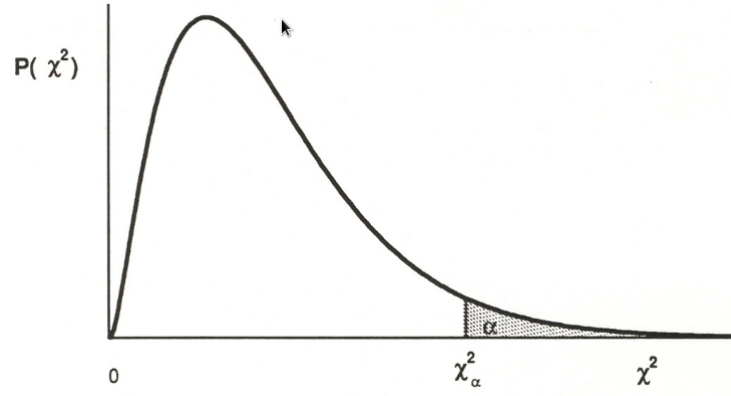
Fig. 4.2 Illustration of the χ^2 distribution used for the limit estimation
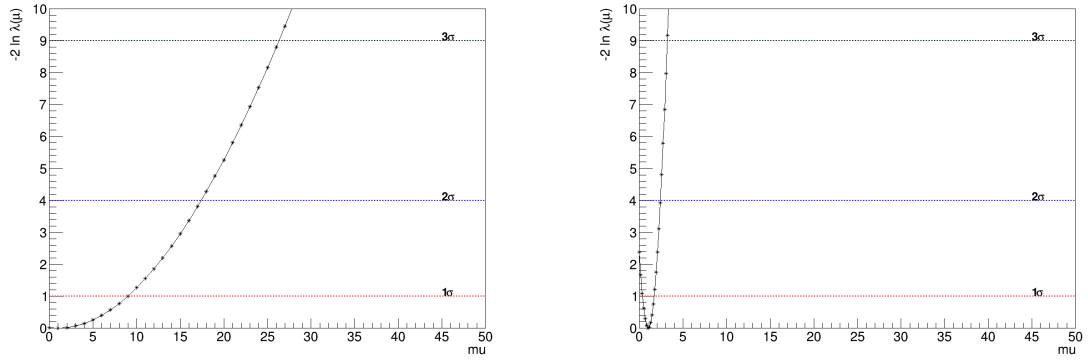

Fig. 4.3 Likelihood scan for SM (Left) and k_t=-1 (Right).

4.3   Extrapolation for higher luminosities

In the past section, it was shown that the signal strength with an integrated luminosity of 35.9fb^{-1} is not significant. The LHC has already collected data for integrated luminosity of 150fb^{-1} for run 2 finished in 2018. Run 3 that starts in 2021 and is expected an integrated luminosity of 300fb^{-1} and for finally the high luminosity phase of LHC , is expected to collect 3000 fb . Therefore, is interesting to study the sensibility of the signal strength and backgrounds to higher luminosities. An extrapolation (scale) is applied to the Asimov data, where it generates new Asimov data that after it is applied an fit and a likelihood scan. For a integrated luminosity of $150fb^{-1}$, $300fb^{-1}$ and $3000fb^{-1}$ in the SM model, the results are the following
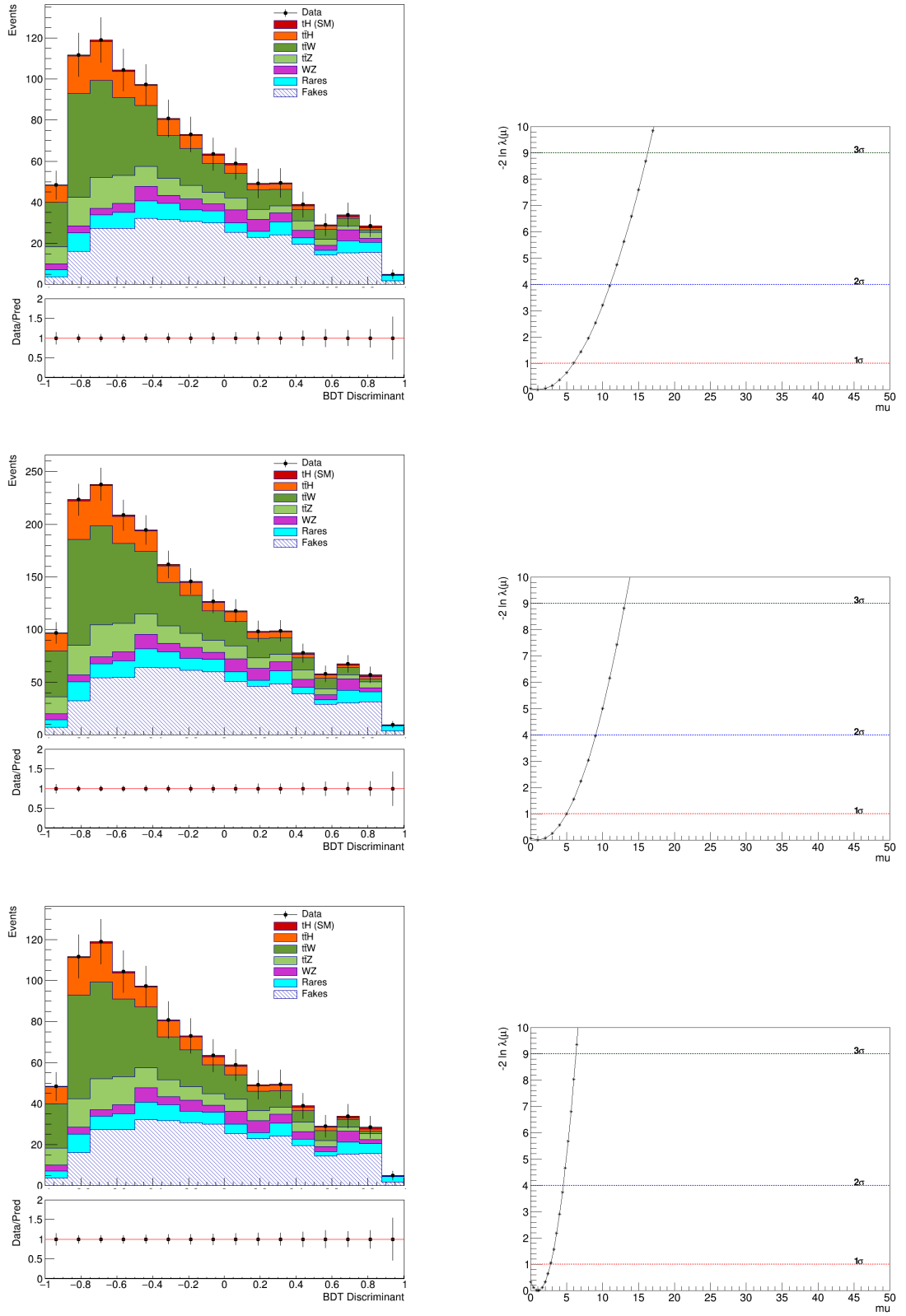
Fig. 4.4 Fit and likelihood scan for 150 fb^{-1}, 300 fb^{-1} and 3000 fb^{-1} in SM model.

461   In the figures 4.4, it is shown an estimated prediction of the signal and background
462 events for higher luminosities. As the luminosity increases, the number of events for both
463 signal and backgrounds also increases, as previously explained in the chapter 1. But even
464 with the increase of number of events, the ratio of signal and data is still very small, with
465 a slightly increase in the ratio in the 3000 fb $^{-1}$ case. In the likelihood scan for higher
466 luminosities, as the luminosity increases, the signal strength μ value starts to decrease and
467 so its uncertainty. This is caused by the increased events available for the fit.
468

469   The same method is used for the model k_t=-1 in the figure 4.5. In this case, the number
470 of events for the signal is more appreciable in comparison with the SM model, same as the
471 35.9fb $^{-1}$ case. However, the likelihood scan parabolas are very closed and that indicates a
472 decrease in the uncertainty of μ more notable than SM case. For the 3000 fb $^{-1}$ case, the
473 curve closes in $\mu \approx 2$. Of course, as the previous section, we estimate the upper limit for
474 these cases and they are shown in the table 4.3

Table 4.3 Estimation of μ and upper limits for Asimov extrapolations for SM and k_t=-1
models.

Luminosity (fb $^{-1}$)	μ	μ upper limit	μ for $k_t = -1$	μ upper limit for $k_t = -1$
35.9	1.00 ± 7.7	17.0	1.0 ± 0.5	2.3
150	1.00 ± 6.7	10.7	1.0 ± 0.4	1.8
300	1.00 ± 4.3	8.7	1.0 ± 0.3	1.5
3000	1.00 ± 1.75	4.3	1.0 ± 0.1	1.1

475   The table shows the upper limits of μ for both models and different luminosities.
476 For the SM case, the uncertainties in μ are greater than the k_t=-1 case. The increase of
477 luminosity reduces the uncertainty of μ that is visualized in the likelihood graphs. The
478 upper limits reduces as the luminosity increases; from 150 to 3000 fb $^{-1}$, the upper limit
479 reduces in $\Delta\mu$=12.7 with $\Delta\mu$ the change of μ . However, the uncertainty of μ for the
480 SM case is still very big, with a error of 75 % in the 3000 fb $^{-1}$ case, indicating that it
481 is necessary to increase the luminosity even higher to get better results and reduce the
482 uncertainty of μ and increase the signal data ratio .
483

484 In the k_t=-1 model the uncertainty of μ decreases with higher luminosities giving better
485 results; upper limits in this models are small , so reducing the incompatibility of model
486 with the data. Changing upper limit values are less notorious than SM case; the value
487 decreases in around $\Delta\mu$=1.2. This is caused by the fact that the uncertainty of k_t=-1 model
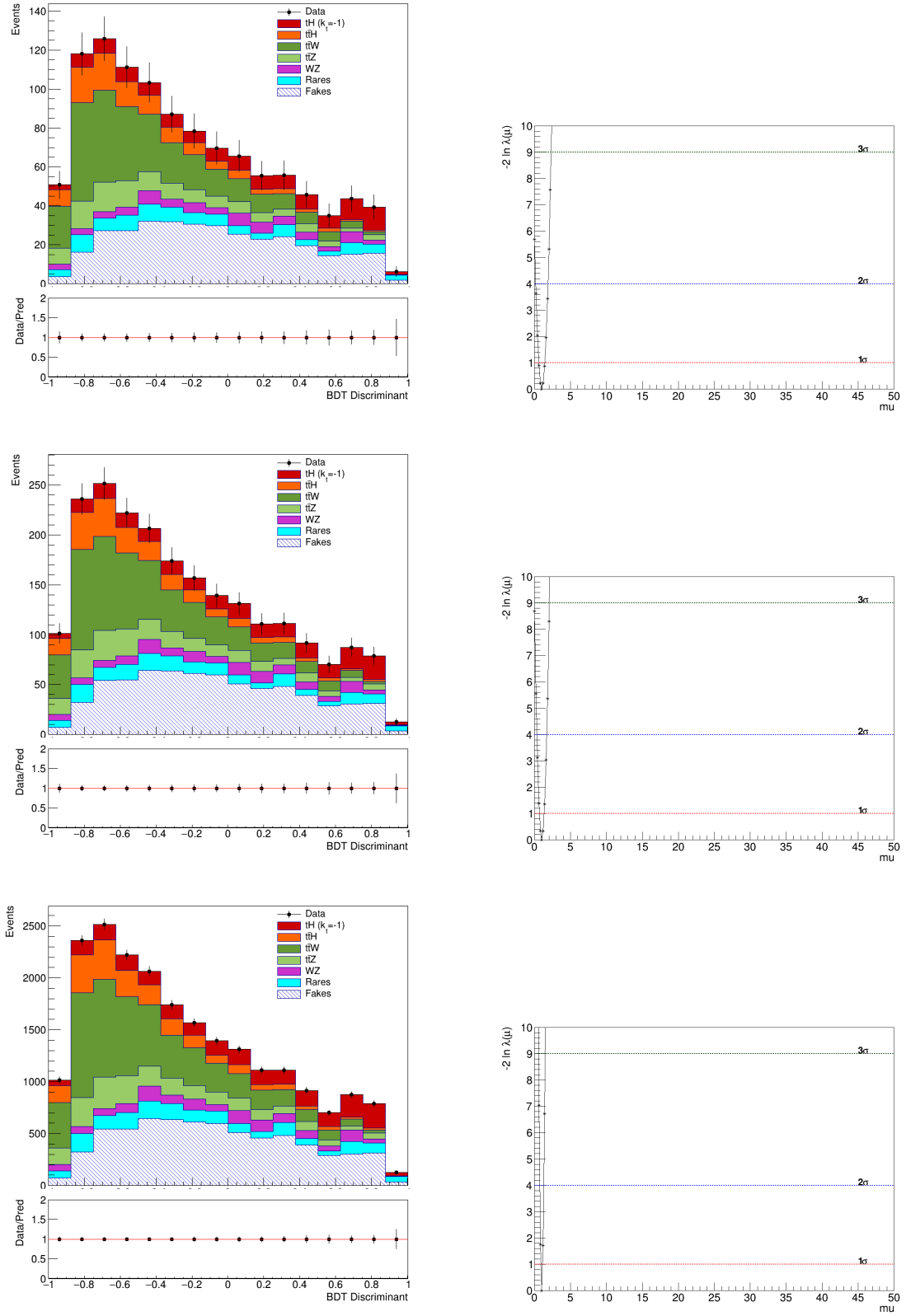488 has a lower uncertainty than the SM model and the number of events for the tH signal is
489 greater.

Fig. 4.5 Fit and likelihood scan for 150fb^{-1}, 300fb^{-1} and 3000fb^{-1} in SM model.

Chapter 5

Conclusion and outlook

References

[1] Search for the tH(H→ bb̄) process in pp collisions at $\sqrt{s} = 13\,\text{TeV}$ and study of Higgs boson couplings. Technical Report CMS-PAS-HIG-17-016, CERN, Geneva, 2018.

[2] O. Brüning P. Fessia M. Lamont L. Rossi L. Tavian G. Apollinari, I. Béjar Alonso. High-luminosity large hadron collider (hl-lhc). technical design report v. 0.1,. *CERN Yellow*, (CERN-2017-007-M), 2017.

[3] G L Bayatian, S Chatrchyan, and Et Al. Hmayakyan. *CMS Physics: Technical Design Report Volume 1: Detector Performance and Software*. Technical Design Report CMS. CERN, Geneva, 2006.

[4] L.D. Landau y E.M. Lifschitz. *Mechanics*, volume 3 of *Course of Theoretical Physics*. Butterworth Heinemann, third edition, 1966.

[5] Frank Gross. *Relativistic quantum mechanics and field theory*. WllEY-VCH Verlag GmbH Co. KGaA, first edition, 1998.

[6] Tanabashi M. Et Al. *Review of Particle Physics*, volume 98. American Physical Society, Aug 2018.

[7] D.J. Griffiths. *Introduction to elementary particles*. WllEY-VCH Verlag GmbH Co. KGaA, second edition, 2008.

[8] Mark Thompson. *Modern particle physics*. Cambridge University press, first edition, 2013.

[9] Chatrchyan et al. Observation of a new boson at a mass of 125 gev with the cms experiment at the lhc. *Physics Letters B*, 716(1):30 – 61, 2012.

[10] Stephen Parke Tom Schwarz Frédéric Déliot, Nicholas Hadley. Properties of top quark. *arXiv.org*, (arXiv:1803.00656):45, 2018.

[11] The CMS Collaboration. Search for production of a higgs boson and a single top quark in multilepton final states in proton collisions at $\sqrt{s}$ = 13 tev. *The CMS Collaboration*, (CMS PAS HIG-17-005), May 2017.

[12] S. Dawson. Introduction to electroweak symmetry breaking. *arXiv.org*, (arXiv:hep-ph/9901280):30, 1999.

[13] PAUL LANGACKER. Introduction to the standard model and electroweak physics. *arXiv.org*, (arXiv:0901.0241):45, 2009.

[14] LHC experiment. The large hadron collider. https://home.cern/science/accelerators/large-hadron-collider, 2019.

[15] CMS experiment. The cms detector. https://cms.cern/detector, 2019.

[16] The CMS collaboration. The performance of the cms muon detector in proton-proton collisions at $\sqrt{s}$= 7 tev at the lhc. *Journal of Instrumentation*, 8(11):P11002–P11002, nov 2013.

[17]

[18] Eilam Gross Ofer Vitells Glen Cowan, Kyle Cranmer. Asymptotic formulae for likelihood-based tests of new physics. *arXiv.org*, (arXiv:1007.1727v3):32, 2013.

[19] Charles Poole Herbert Goldstein and John Safko. *Classical Mechanics*. Addison Wesley Longman Inc., 3 edition, 2002.

Appendix A

Scattering and cross section

In classical mechanics, scattering is a set of particles which deviate from their original trajectory to one or many ways. Examples of scattering are particle collisions and particles that deviates in a potential field.

The cross section in a scattering is the area transverse to the relative motion between two object to scatter from each other.[19] For a particle which deviates from its original way due to a potential whose center is at rest, the scattering angle is given by

$$\theta = \pi - 2\phi_0 \tag{A.1}$$

with

$$\phi_0 = \int_{r_0}^{\infty} \frac{M/r^2 dr}{\sqrt{2m(E - U(r) - M^2/r^2}} \tag{A.2}$$

with r_0 the nearest position to the center of potential and $U(r)$ is the potential. Now for great velocity , if we change $E = \frac{1}{2}mv^2$ and $M = mpv$ and substitute in A.2, we have

$$\phi_0 = \int_{r_0}^{\infty} \frac{\rho/r^2 dr}{\sqrt{1 - \frac{\rho^2}{r^2} - 2U(r)/mv^2}} \tag{A.3}$$

in terms of parameter of impact ρ and the position[4]. In a scattering of a beam of identical particles with velocity of v , let dN the number of particles scattered per unit of time through the angles θ and $\theta + d\theta$ The effective cross section is
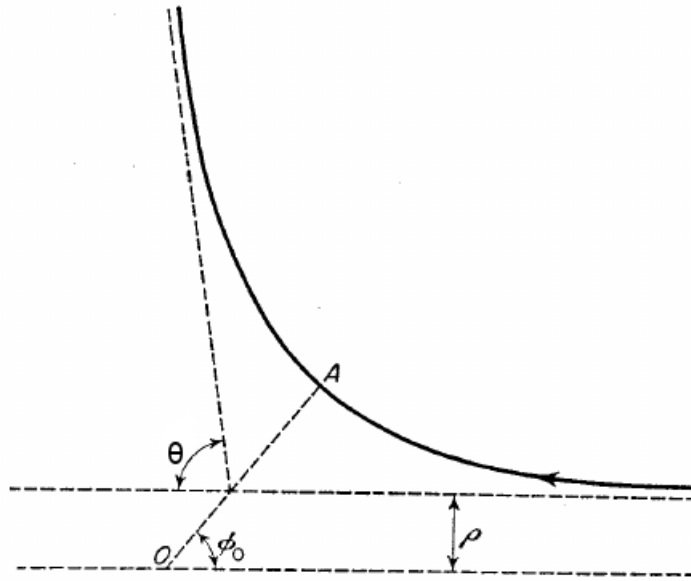
$$d\sigma = \frac{dN}{n} \tag{A.4}$$

Fig. A.1 Diagram of scattering for a particle in a potential field[4]

n represents the number of particles passing in unit of time in a unit area of beam cross section. If ρ is θ dependient, then the effective cross section is

$$dN = 2\phi\rho n d\rho \qquad d\sigma = 2\phi\rho d\rho \qquad (A.5)$$

rewriting $d\sigma$

$$d\sigma = 2\phi\rho \left| \frac{d\rho}{d\theta} \right| d\theta \qquad (A.6)$$

the derivative $\frac{d\rho}{d\theta}$ can be negative ,so it is necessary the modulus [4]. In a three dimension model, $d\sigma$ is related to the solid angle, instead of $d\theta$, so the solid angle between the angles θ and $\theta + d\theta$ is

$$d\Omega = 2\pi \sin\theta d\theta \qquad (A.7)$$

thus, the cross section is

$$d\sigma = \frac{\rho(\theta)}{\sin\theta} \left| \frac{d\rho}{d\theta} \right| d\Omega \qquad (A.8)$$
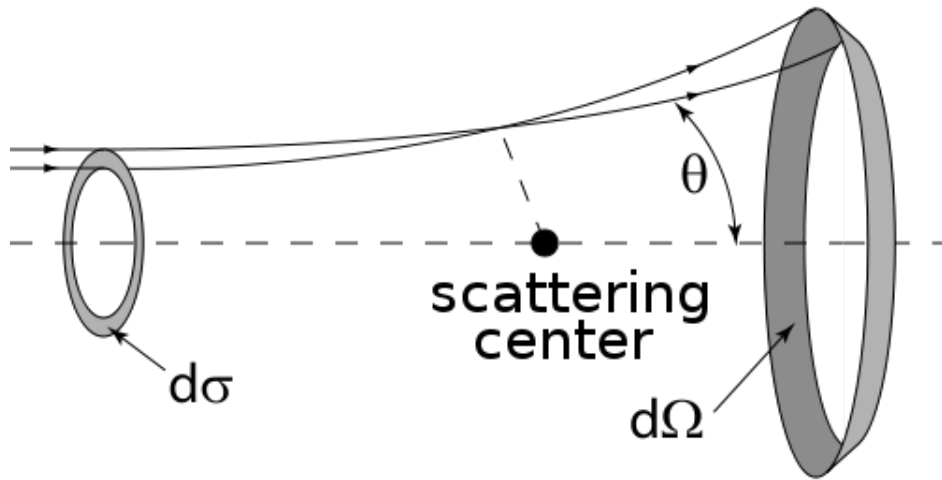
Fig. A.2 Drawing of an idealized scattering process showing the differential solid angle $\Delta\Omega$ and the scattering angle θ [5]

let N be the number of events. In terms of of solid angle

$$dN = \mathrm{L}d\sigma = \mathrm{L}\frac{d\sigma}{d\Omega}d\Omega \qquad \frac{d\sigma}{d\Omega} = \frac{dN}{\mathrm{L}d\Omega} \tag{A.9}$$

For a collision of two particles that produce many particles, the cross section is given by

$$\sigma = \frac{S\hbar^2}{4\sqrt{(p_1 \cdot p_2)^2 - (m_1 m_2 c^2)^2}} \int |M|^2 (2\pi)^4 \delta^4(p_1 - p_2 - \ldots p_n) \times \prod_{j=2}^{n} 2\pi\delta(p_j^2 - m_j^2 c^2)\theta(p_j^0)\frac{d^4 p_j}{(2\pi)^4} \tag{A.10}$$

the structure of the equation A.10 is similar to the equation ??[7].

Experimentally

$$d\sigma = \frac{\text{number of particles scattered into solid angle}\Delta\Omega}{(\text{number of particles incident})(\text{scattering centers/area})} \tag{A.11}$$